

Systematic single-folding model nucleus-nucleus potential for peripheral collisions

G. Yang ^{1,2} D. Y. Pang ^{3,*} Y. Y. Yang ^{1,2,†} K. Wang ^{1,2} F. F. Duan, ¹ X. X. Wang, ^{1,4} and Z. Y. Sun ^{1,2}

¹Institute of Modern Physics, Chinese Academy of Sciences, Lanzhou 730000, China

²School of Nuclear Science and Technology, University of Chinese Academy of Sciences, Beijing 100080, China

³School of Physics and Beijing Key Laboratory of Advanced Nuclear Materials and Physics, Beihang University, Beijing 100191, China

⁴College of Physics and Electronic Engineering, Northwest Normal University, Lanzhou 730070, China



(Received 28 February 2022; accepted 23 February 2023; published 7 April 2023)

A systematic nucleus-nucleus potential for the ${}^9\text{Be}$ projectile is derived by analyzing its elastic scattering on target nuclei from ${}^{16}\text{O}$ to ${}^{209}\text{Bi}$ with incident energies ranging from 12 to 202 MeV. The analysis is performed by using a single-folding model based on the Bruyères Jeukenne-Lejeune-Mahaux model nucleon-nucleus potentials. In combination with the previous systematic potential reported by Xu and Pang [Phys. Rev. C **87**, 044605 (2013)], which was obtained by analyzing the elastic-scattering data of ${}^6\text{Li}$ and ${}^7\text{Li}$ at incident energies above 10 MeV/nucleon, we arrive at an updated systematic nucleus-nucleus potential which covers a range of incident energies from around the Coulomb barrier to about 100 MeV/nucleon. This updated potential is found to satisfy the dispersion relations better than the previous one.

DOI: [10.1103/PhysRevC.107.044603](https://doi.org/10.1103/PhysRevC.107.044603)

I. INTRODUCTION

Optical model potentials (OMP) play an important role in studies of nuclear reaction mechanisms and nuclear structure [1]. They are usually obtained by fitting experimental data of elastic-scattering angular distributions. However, such procedures do not always work. First, experimental data that are needed to constrain the optical model potential parameters are not always available, especially when radioactive nuclei are involved. Another problem lies in the fact that OMP parameters, which are obtained by fitting only one or several sets of experimental data, have rather large uncertainties. For these reasons, systematic OMPs become extremely important since they are constrained by experimental data that cover rather large ranges of target masses and incident energies. This allows the systematic OMPs to have much smaller uncertainties and to be more reliable when being extrapolated to unknown regions. Many studies on the systematic OMPs for light nuclei have been conducted [2–4], but those for heavy ions have been relatively rare.

In recent years, many studies have been performed on systematic nucleus-nucleus potentials. For instance, great success has been achieved for both stable and unstable particles when applying a global description of the nucleus-nucleus (AA) interactions developed by Chamon *et al.* in a simple way through a double-folding shape (the São Paulo potential, SPP) [5] by taking into account the Pauli nonlocal nature of the interaction [6,7]. Furumoto *et al.* proposed a new global AA potential through a microscopic folding model with the complex G -matrix interaction and systematic São Paulo

density for neutron-rich and proton-rich isotopes [8]. Global phenomenological optical model potentials for both weakly bound and tightly bound nuclei have also been obtained, for instance, in Refs. [9–11].

Recently, a systematic nucleus-nucleus potential based on the Bruyères Jeukenne-Lejeune-Mahaux (JLMB) model nucleon-nucleus potential has been proposed [12]. It has been found to account for the elastic scattering of not only stable nuclei, such as ${}^9\text{Be}$ [13] and ${}^{10}\text{B}$ [14], but also of radioactive nuclei, such as ${}^7\text{Be}$, ${}^8\text{B}$, ${}^{9-11}\text{C}$, and ${}^{10}\text{Be}$ [13–16]. However, parameters of this potential were determined by fitting the experimental elastic-scattering angular distribution data of ${}^6,{}^7\text{Li}$ at incident energies well above the Coulomb barriers. An extension of this systematic potential to lower incident energies will be very useful. ${}^9\text{Be}$, which is the only β -stable nucleus of the beryllium isotopes, has been studied extensively. Experimental data of its elastic-scattering angular distributions are available within a wide range of incident energies on various targets. This allows us to extend the systematic OMP to low energies down to the vicinity of the Coulomb barriers. By combining results of the present work and those of Ref. [12], we arrive at a systematic nucleus-nucleus potential that is applicable for incident energies from near to the Coulomb barrier to around 100 MeV/nucleon. This extension not only makes the potential more useful but also allows one to examine the dispersion relations of the real and imaginary parts of this systematic optical model potential.

The organization of this paper is as follows. In Sec. II, the formalism used in the present work is described. It is followed by a description of the analysis of the elastic-scattering data, with which renormalization factors (RFs) of the real and imaginary potentials of ${}^9\text{Be}$ are derived. The systematics of these RFs, namely, their dependence on the incident energies, are combined with those of ${}^6,{}^7\text{Li}$ to obtain a new systematic

*Corresponding author: dypang@buaa.edu.cn

†Corresponding author: yangyanyun@impcas.ac.cn

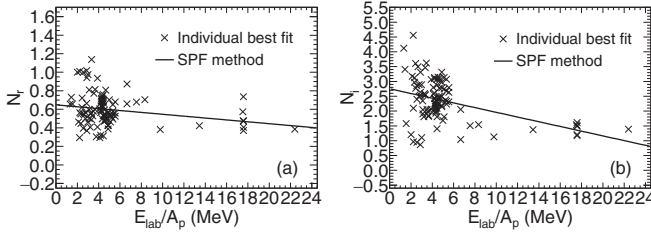


FIG. 1. Renormalization factors for (a) N_r and (b) N_i from individual fits of ${}^9\text{Be}$ elastic scattering. The solid lines represent the linear functions of Eqs. (5) and (6).

potential. Examination of this new potential is made by comparing the theoretical and experimental elastic-scattering and total-reaction cross sections (σ_R) for various projectile-target systems at different incident energies. Discussion on the consistency with the dispersion relations is presented in Sec. IV. Finally, a summary of the results and the conclusions are presented in Sec. V.

II. THE SINGLE-FOLDING NUCLEUS-NUCLEUS POTENTIAL

The nucleus-nucleus potential $U(R, E_{\text{lab}})$, which is a function of the distance between the centers of masses of the projectile and the target nuclei, R , is considered to be dependent on the incident energy E_{lab} and consists of both a nuclear part [$U_N(R, E_{\text{lab}})$] and a Coulomb part [$V_C(R)$]:

$$U(R, E_{\text{lab}}) = U_N(R, E_{\text{lab}}) + V_C(R). \quad (1)$$

The Coulomb part is

$$V_C(R) = \begin{cases} \frac{Z_p Z_T e^2}{r} & (r > R_C), \\ \frac{Z_p Z_T e^2}{2R_C} \left[3 - \frac{r^2}{R_C^2} \right] & (r \leq R_C), \end{cases} \quad (2)$$

where the charge radius $R_C = 1.3 \times (A_P^{1/3} + A_T^{1/3})$ fm, with A_P and A_T being the mass numbers of the projectile and the

TABLE I. The values of parameters for Eqs. (5), (6), (8), and (9).

Parameter	SPF	SMF	ASMF
t_r	0.647979	0.58672	0.601794
k_r	-0.010156	-0.010087	-0.00864214
t_i	2.75257	2.5869	2.53345
k_i	-0.0795331	-0.074843	-0.0717581
a_r	0.99999	0.99999	0.999995
b_r	-0.00592095	-0.00585195	-0.00440712
c_r	0.000207097	0.000205116	0.000165819
d_r	0.000207095	0.000205114	0.000165818
a_i	0.998425	0.998605	0.998715
b_i	-0.0794077	-0.0747385	-0.071666
c_i	0.00630559	0.00558584	0.00513601
d_i	0.00629565	0.00557804	0.00512942
x_0^r	15.6611	11.4593	13.9157
y_0^r	0.488925	0.47113	0.481533
x_0^i	19.2746	18.2689	18.3094
y_0^i	1.2196	1.2196	1.2196

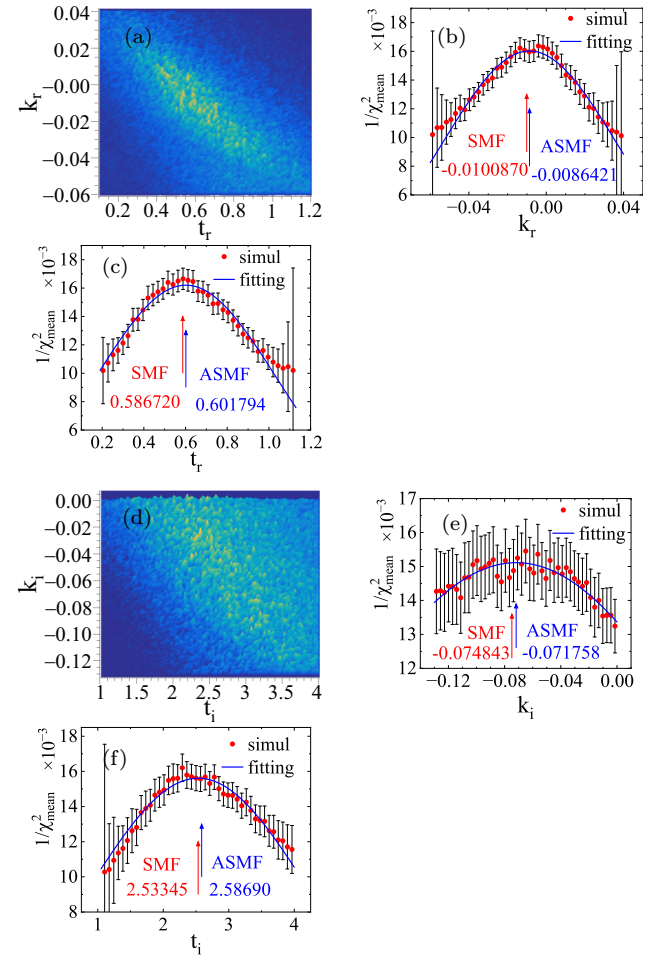


FIG. 2. Three-dimensional plots of the slope and intercept parameters and their associated $1/Q^2$ values for the real part (a) and the imaginary part (d), as well as their projections on the slope axis [panels (b) and (c)] and the intercept axis [panels (e) and (f)], respectively.

target, respectively. The nuclear part of the OMP is calculated with the single-folding model [12]:

$$U_{\text{sf}}(R, E_{\text{lab}}) \equiv \sum_{i=p,n} \int \rho_i(\mathbf{r}) v(E_i, |\mathbf{s}|) d\mathbf{r}, \quad (3)$$

where $\rho_i(\mathbf{r})$ is the nucleon ($i = p$ for proton and $i = n$ for neutron) density distribution in the projectile at position \mathbf{r}

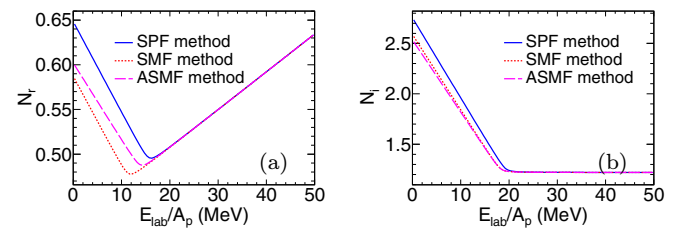


FIG. 3. Energy dependence of (a) N_r and (b) N_i . The solid lines, dotted lines, and dashed lines are the results of SPF, SMF, and ASMF methods, respectively, with the function forms of Eqs. (8) and (9).

TABLE II. Experimental data analyzed in the present work for ^9Be on different targets, their references, and their corresponding Q^2 values calculated with the systematic parameters of the SMF, ASMF, and SPF methods. The incident energies E_{lab} are in MeV.

Target	E_{lab}	Q^2_{SMF}	Q^2_{ASMF}	Q^2_{SPF}	Ref.
^{16}O	20.00	9.645	8.063	8.741	[37]
^{16}O	25.94	29.73	30.45	29.20	[37]
^{16}O	27.00	49.98	49.66	49.16	[38]
^{16}O	40.00	44.87	44.45	45.79	[38]
^{16}O	157.7	224.3	224.4	207.8	[39]
^{26}Mg	158.3	4939	5003	2493	[39]
^{27}Al	12.00	0.8892	0.8155	0.7034	[40]
^{27}Al	14.00	1.431	1.164	0.8708	[40]
^{27}Al	18.00	34.87	30.70	29.19	[40]
^{27}Al	22.00	0.8960	0.6333	0.5503	[40]
^{27}Al	25.00	0.3137	0.3013	0.2891	[40]
^{27}Al	28.00	11.93	9.399	10.09	[41]
^{27}Al	32.00	13.38	10.83	11.57	[41]
^{27}Al	33.00	21.42	18.19	19.08	[41]
^{27}Al	35.00	6.642	5.551	6.255	[40]
^{27}Al	158.2	27.62	27.98	19.03	[39]
^{28}Si	13.00	0.5681	0.5118	0.3283	[42]
^{28}Si	20.00	11.69	9.111	9.701	[43]
^{28}Si	23.00	5.685	4.569	4.492	[43]
^{28}Si	26.00	3.551	2.567	2.501	[43]
^{28}Si	30.00	13.33	11.33	12.22	[43]
^{28}Si	121.0	209.5	225.9	366.3	[42]
^{28}Si	201.6	438.1	439.0	433.9	[42]
^{40}Ca	45.00	131.0	104.5	122.2	[34]
^{40}Ca	60.00	2.561	2.362	2.259	[34]
^{40}Ca	158.1	63.55	64.01	55.54	[39]
^{60}Ni	158.2	189.9	190.1	198.9	[39]
^{64}Zn	19.00	0.2314	0.2330	0.2643	[44]
^{64}Zn	21.00	0.9926	1.217	1.934	[44]
^{64}Zn	23.00	3.636	4.276	5.556	[44]
^{64}Zn	26.00	8.523	9.793	11.01	[44]
^{64}Zn	28.00	1.596	1.783	2.187	[44]
^{64}Zn	28.97	1.795	2.373	3.033	[45]
^{80}Se	19.94	0.2912	0.2809	0.1800	[46]
^{80}Se	20.94	0.1665	0.1434	0.1172	[46]
^{80}Se	21.94	1.433	1.223	0.7495	[46]
^{80}Se	22.94	0.7590	0.8612	1.113	[46]
^{80}Se	23.95	1.051	1.093	1.211	[46]
^{80}Se	24.95	0.8324	1.057	1.430	[46]
^{80}Se	29.95	1.470	1.685	1.841	[46]
^{80}Se	32.76	10.39	8.533	7.951	[46]
^{120}Sn	25.96	0.2500	0.2435	0.1444	[24]
^{120}Sn	26.93	0.07795	0.07483	0.09748	[24]
^{120}Sn	27.97	0.1324	0.1259	0.2396	[24]
^{120}Sn	29.44	0.3503	0.4084	0.7510	[24]
^{120}Sn	30.97	1.241	1.272	1.451	[24]
^{120}Sn	41.96	12.97	11.13	9.653	[24]
^{120}Sn	49.96	5.737	5.923	5.634	[24]
^{144}Sm	30.00	0.02507	0.02535	0.02773	[47]
^{144}Sm	31.50	0.05514	0.05672	0.1444	[47]
^{144}Sm	34.00	4.794	5.156	7.077	[48]
^{144}Sm	35.00	3.936	4.523	6.881	[48]
^{144}Sm	37.00	10.98	12.38	15.53	[48]
^{144}Sm	39.00	1.811	2.278	3.470	[48]
^{144}Sm	41.00	2.370	2.937	4.006	[48]

TABLE II. (Continued.)

Target	E_{lab}	Q^2_{SMF}	Q^2_{ASMF}	Q^2_{SPF}	Ref.
^{144}Sm	44.00	0.4654	0.3975	0.5096	[47]
^{144}Sm	48.00	2.549	1.587	1.145	[47]
^{197}Au	36.94	0.2329	0.2307	0.09764	[49]
^{197}Au	37.94	0.9414	0.8980	0.4030	[49]
^{197}Au	38.94	0.2920	0.2465	0.06315	[49]
^{197}Au	39.94	0.4256	0.3281	0.1402	[49]
^{197}Au	40.94	0.7246	0.6316	0.5179	[49]
^{197}Au	41.95	0.6219	0.4941	0.4906	[49]
^{197}Au	43.95	1.514	1.252	0.8842	[49]
^{197}Au	45.95	3.120	3.388	3.687	[49]
^{197}Au	47.95	1.111	0.8313	0.4354	[49]
^{197}Au	158.2	22.35	22.26	27.10	[39]
^{208}Pb	37.8	0.08649	0.08665	0.02263	[35]
^{208}Pb	38.00	0.08339	0.08206	0.01688	[35]
^{208}Pb	38.20	0.08977	0.08659	0.02352	[35]
^{208}Pb	38.50	0.1614	0.1524	0.02920	[35]
^{208}Pb	38.70	0.09541	0.08701	0.03522	[35]
^{208}Pb	39.00	0.1787	0.1615	0.03201	[35]
^{208}Pb	39.50	0.2629	0.2262	0.03525	[35]
^{208}Pb	40.00	0.1348	0.1072	0.3140	[50]
^{208}Pb	40.00	0.2667	0.2180	0.04164	[35]
^{208}Pb	41.00	0.1507	0.1508	0.3387	[35]
^{208}Pb	42.00	0.3407	0.4841	1.324	[50]
^{208}Pb	42.00	0.5315	0.7062	1.483	[35]
^{208}Pb	44.00	1.822	2.499	4.347	[50]
^{208}Pb	44.00	3.801	4.489	6.123	[35]
^{208}Pb	46.00	1.623	2.056	3.127	[35]
^{208}Pb	47.20	2.328	3.368	4.904	[50]
^{208}Pb	48.00	0.7757	1.175	2.079	[35]
^{208}Pb	50.00	0.5136	0.3657	0.5319	[50]
^{208}Pb	50.00	4.057	5.248	6.257	[35]
^{208}Pb	60.00	2.674	1.605	0.8385	[50]
^{208}Pb	68.00	15.86	12.17	10.06	[50]
^{208}Pb	75.00	19.71	15.49	13.51	[50]
^{208}Pb	88.00	0.2066	0.2103	0.2039	[51]
^{209}Bi	37.80	0.07867	0.08134	0.02590	[35]
^{209}Bi	38.00	0.03673	0.03746	0.01528	[35]
^{209}Bi	38.20	0.03126	0.03098	0.01333	[35]
^{209}Bi	38.50	0.05248	0.05042	0.01394	[35]
^{209}Bi	38.70	0.04172	0.03900	0.01355	[35]
^{209}Bi	39.00	0.07073	0.06384	0.02211	[35]
^{209}Bi	39.50	0.09631	0.08179	0.02767	[35]
^{209}Bi	40.00	0.3867	0.3873	0.3817	[52]
^{209}Bi	40.00	0.1670	0.1383	0.03708	[35]
^{209}Bi	41.00	0.1219	0.1137	0.2469	[35]
^{209}Bi	42.00	1.398	1.166	0.5136	[52]
^{209}Bi	42.00	0.3223	0.4276	1.018	[35]
^{209}Bi	44.00	1.161	1.254	1.687	[52]
^{209}Bi	44.00	2.938	3.517	4.999	[35]
^{209}Bi	46.00	1.399	1.547	1.926	[52]
^{209}Bi	48.00	2.724	2.540	2.337	[52]

from the center of mass (c.m.) of the projectile, $E_i = E_{\text{lab}}/A_P$ is the incident energy per nucleon, and $\mathbf{s} = \mathbf{R} + \mathbf{r}$ is the vector from the c.m. of the target to that nucleon. $v(E_i, |\mathbf{s}|)$ is the interaction between a free nucleon and the target nucleus, which is chosen to be the semimicroscopic Lane-consistent

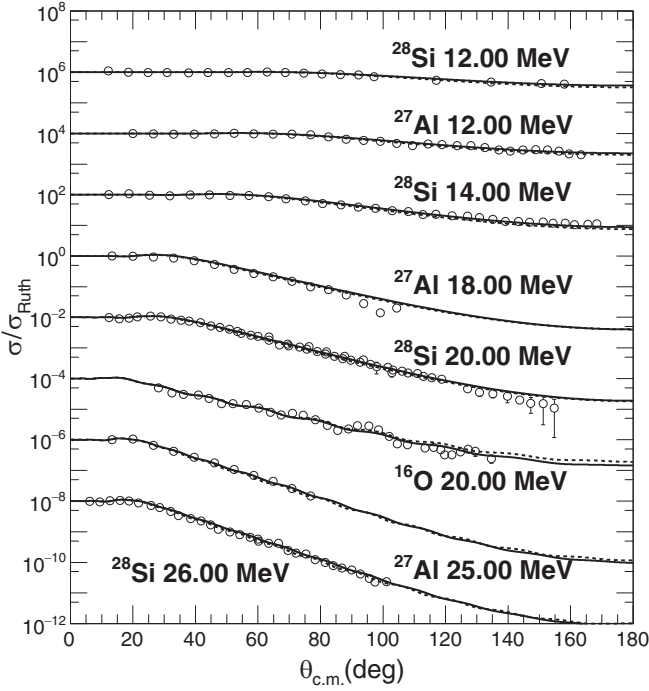


FIG. 4. Comparisons between optical model calculations and experimental data for ^9Be elastic scattering from ^{16}O , ^{27}Al , and ^{28}Si at incident energies indicated in the figure. The solid and dashed curves represent results calculated with the systematic potential of this work and with SPP2, respectively. The data sets are offset for optimum view. The experimental data are from Refs. [37,40,43].

JLMB model potential [17,18] in this work. The calculation of $v(E_i, |s|)$ involves applying the local density approximation to the nucleon potential of infinite nuclear matter to obtain the one of a finite target nucleus. The details of which can be found in Refs. [4,17,18].

Being based on a free nucleon-target optical model potential, the single-folding model nucleus-nucleus potential calculated in Eq. (3) needs to be renormalized to account for the medium effects of the nucleons in the projectile nucleus [19]. This is made by introducing renormalization factors to the real and imaginary parts of the single-folding potential. So now the nuclear part of the optical potential is

$$U_N(R, E_{\text{lab}}) = N_r \text{Re}[U_{\text{sf}}] + N_i \text{Im}[U_{\text{sf}}]. \quad (4)$$

The renormalization factors N_r and N_i are the parameters to be determined by comparing with the experimental data.

In this work, we study how the N_r and N_i values depend on the incident energies based on the elastic-scattering data of the ^9Be projectile. It is an extension of Ref. [12], in which the experimental data of ^6Li and ^7Li elastic scattering were analyzed for incident energies well above the Coulomb barriers. The current work focuses on incident energies at around the Coulomb barrier. ^9Be is chosen because there are a lot of experimental data available at the energies we are interested in. As we demonstrate in the following, the systematics of N_r and N_i obtained with the ^9Be data can be applied satisfactorily to many other nuclei. Spin-orbit potentials are neglected although ^9Be has a nonzero spin. This is because the elastic

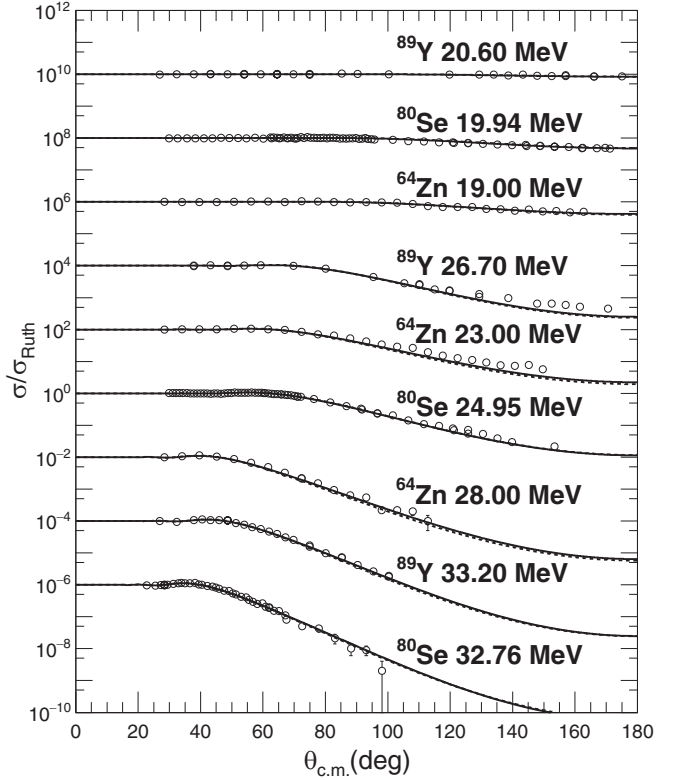


FIG. 5. Same as Fig. 4, but for ^{64}Zn , ^{80}Se , and ^{89}Y targets. The experimental data are from Refs. [44,46,53].

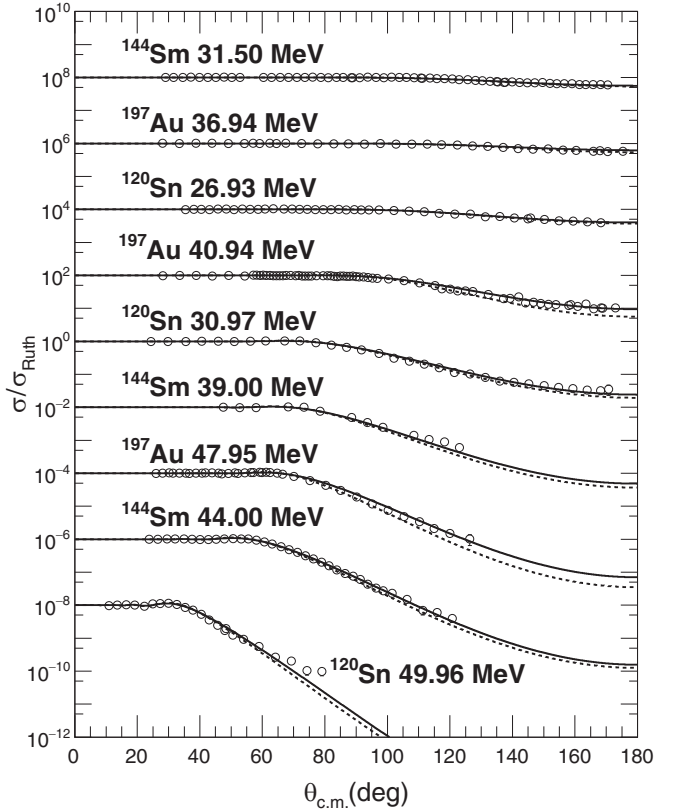


FIG. 6. Same as Fig. 4, but for ^{120}Sn , ^{144}Sm , and ^{197}Au targets. The experimental data are from Refs. [24,47–49].

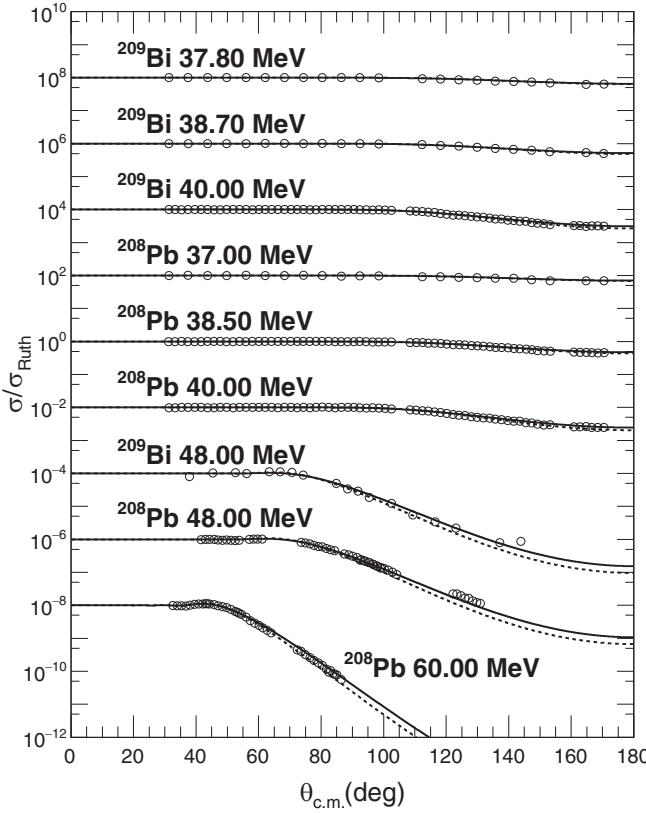


FIG. 7. Same as Fig. 4, but for ^{208}Pb and ^{209}Bi targets. The experimental data are from Refs. [35,50,52].

angular distribution data analyzed in this work are not sensitive to the spin-orbit potentials. From a practical point of view, spin-orbit potentials are usually not important for describing heavy-ion-heavy-ion scattering [20]. It is also worth mentioning that ^9Be is a weakly bound nucleus whose neutron separation energy is only 1.57 MeV for three-body breakup into $\alpha + \alpha + n$ and 1.67 MeV for breakup into $^8\text{Be} + n$. So breakup coupling effects are important in reactions induced by ^9Be . Many works have been carried out to describe the elastic scattering of ^9Be within the framework of the continuum discretized coupled-channel method [21–27]. The one-neutron transfer reaction channel has also been found to have visible effects on the elastic scattering of ^9Be [28]. These coupling effects are believed to be the reasons for the phenomenological renormalization factors being different from unity [22,28–31]. We do not study these coupling effects explicitly in this work. Instead, we hope the phenomenologically determined renormalization factors reported in this paper could serve as “experimental data” for further analysis with more sophisticated reaction theories.

III. OPTICAL MODEL ANALYSIS

A. The database

The experimental data of elastic-scattering angular distributions for ^9Be on targets whose mass numbers range from 16 to 209 at incident energies between 12 and 202 MeV have been collected from the nuclear reaction database

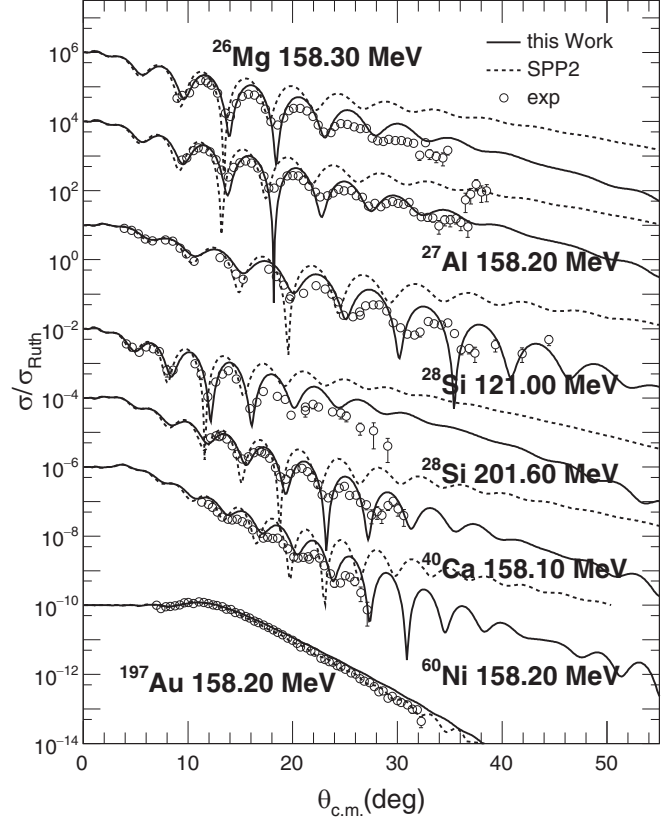


FIG. 8. Same as Fig. 4 but for higher incident energies. The experimental data are from Refs. [39,42].

EXFOR [32] and a nuclear reaction video website [33] except for $^9\text{Be} + ^{40}\text{Ca}$ at $E_{\text{lab}} = 45$ and 60 MeV and $^9\text{Be} + ^{209}\text{Bi}$ at $E_{\text{lab}} = 37$ MeV, which are digitized from Refs. [34,35], respectively. In total, we have 106 sets of elastic-scattering angular distribution data to confine the N_r and N_i values of the single-folding potential.

B. Searching procedures

There are two searching strategies to construct the global potentials, namely, the separate fitting method (SPF) and the simultaneous fitting method (SMF). With the SPF method, each set of angular distribution data was fitted separately to achieve the optimum N_r and N_i values for *this* set of data. Systematic behaviors—the energy dependence of these renormalization factors—were then found by least-square fitting of these individual N_r and N_i values. The SMF method, on the other hand, parametrizes the energy dependence of the RFs *a priori* and searches for the optimum parameters by fitting all the data sets simultaneously. Examples of the SMF method can be found in, e.g., Refs. [2,36]. We try both methods in this work.

1. The separate fitting method

We started the fitting procedure by calculating the nucleus-nucleus potential within the framework of the single-folding model with the RFs whose values were fixed to be unity. The

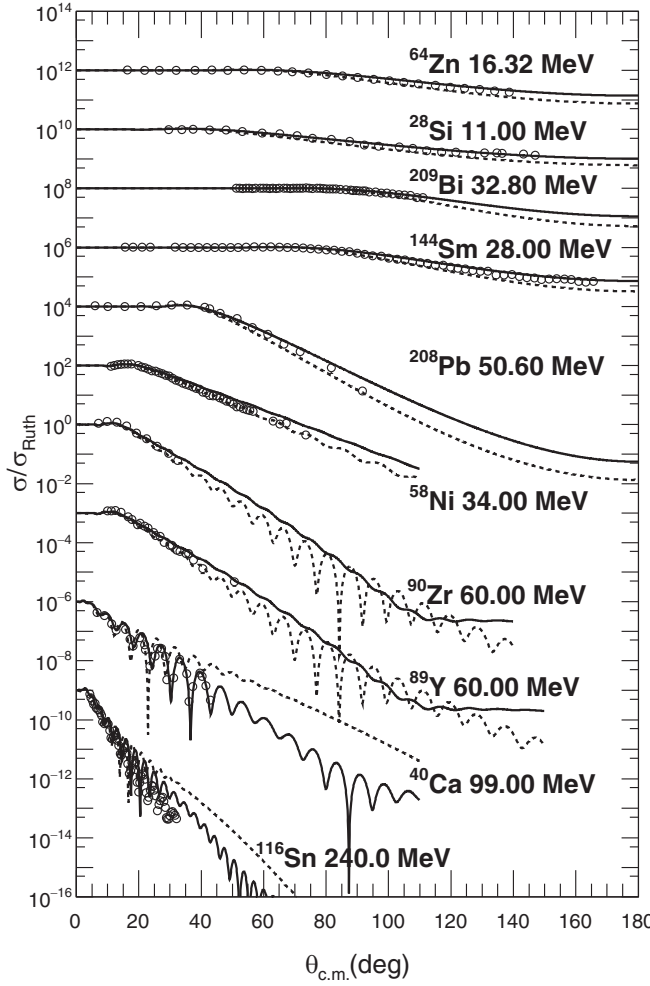


FIG. 9. Comparisons between the optical model calculations and the experimental data of ${}^6\text{Li}$ elastic-scattering angular distributions for several targets at incident energies indicated in the figure. Note that only several representative experimental data have been selected to plot for optimum view. The experimental data are from Refs. [54–62].

created potential for each set of data was fed into the computer code SFRESCO to calculate the elastic-scattering differential cross sections and search for the best values of the RFs. The standard minimum χ^2 (divided by the number of data points) method was used to find the optimum values of N_r and N_i . The distributions of these individual optimum RFs are depicted in Figs. 1(a) and 1(b) for N_r and N_i , respectively, where each symbol represents the optimal value of these parameters from individual fits. As we can see, the scattering of these factors is rather large, especially in the low-energy region. This reflects the fact that the OMP parameters cannot be well confined with single sets of experimental data. Since we do not see any reasons for choosing any particular functions to represent these results, we simply assume that these N_r and N_i values, as a whole, depend linearly on the incident energies, similar to the case with ${}^{6,7}\text{Li}$ (see Fig. 1 in Ref. [12]):

$$N_r = t_r + k_r \times E_{\text{lab}}/A_p, \quad (5)$$

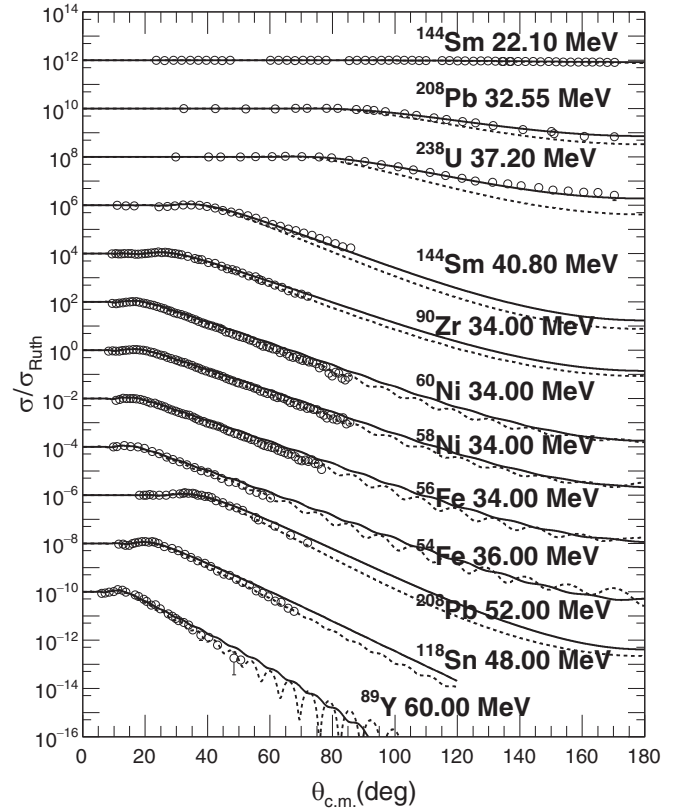


FIG. 10. Same as Fig. 9, but for the ${}^7\text{Li}$ projectile. The experimental data are from Refs. [57,60,63–67].

$$N_i = t_i + k_i \times E_{\text{lab}}/A_p, \quad (6)$$

where E_{lab} is incident energy in the laboratory system and A_p is the mass number of the projectiles. The slope (k_r and k_i) and intercept (t_r and t_i) parameters determined in this way are presented in Table I.

2. The simultaneous fitting method

The very weak constraining power of single sets of experimental data at low energies on the optical potential depths motivated us to use the simultaneous fitting procedure. In this method, we still assume the renormalization factors depend linearly on the incident energies as in Eqs. (5) and (6). The parameters t_r and k_r for the real part and the parameters t_i and k_i for the imaginary part are randomly chosen within $-0.06 \leq k_r \leq 0.04$, $-0.13 \leq k_i \leq 0.0$, $0 \leq t_r \leq 1.2$, and $1.0 \leq t_i \leq 4.0$. These limits are determined by the results in Fig. 1. For each set of $\{t_r, k_r, t_i, k_i\}$ values, we calculate the following quantity:

$$Q^2 = \frac{1}{N} \sum_{i=1}^N \frac{1}{M_i} \sum_{j=1}^{M_i} \left[\frac{\sigma_{ij}^{\text{th}}(\theta_{ij}) - \sigma_{ij}^{\text{exp}}(\theta_{ij})}{\Delta\sigma_{ij}^{\text{exp}}(\theta_{ij})} \right]^2, \quad (7)$$

where N is the total number of angular distribution sets, M_i is the total number of points in the i th set of angular distribution data, σ_{ij}^{exp} is the experimental differential cross section of the j th scattering angle θ_{ij} in the i th set of data, and σ_{ij}^{th} and

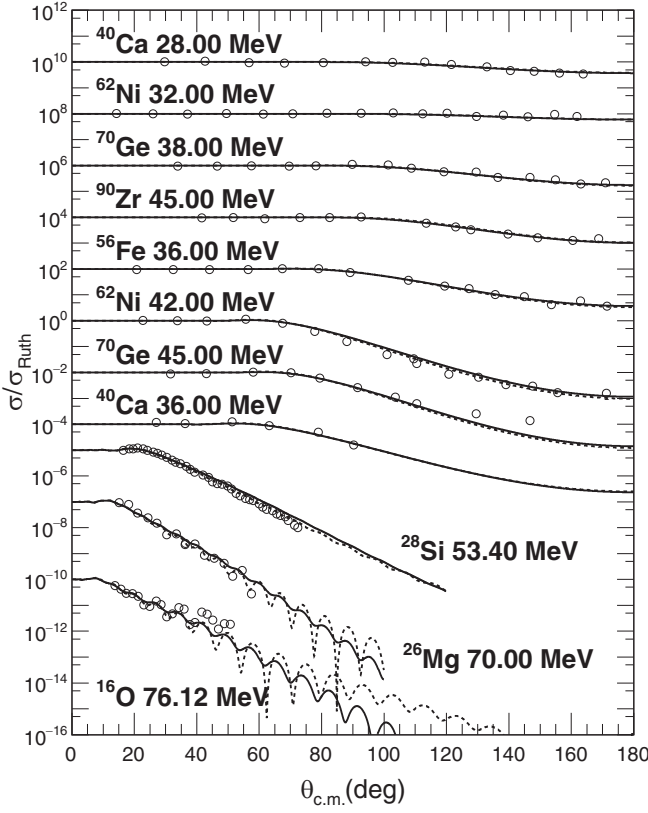


FIG. 11. Same as Fig. 9, but for the ^{14}N projectile. The experimental data are from Refs. [68–71].

$\Delta\sigma_{ij}^{\text{exp}}$ are the corresponding theoretical cross section and the experimental error. A uniform 10% of uncertainty is assumed for all the experimental data.

A total number of 150 000 samples of the parameter set $\{t_r, k_r, t_i, k_i\}$ were made for the 106 sets of angular distri-

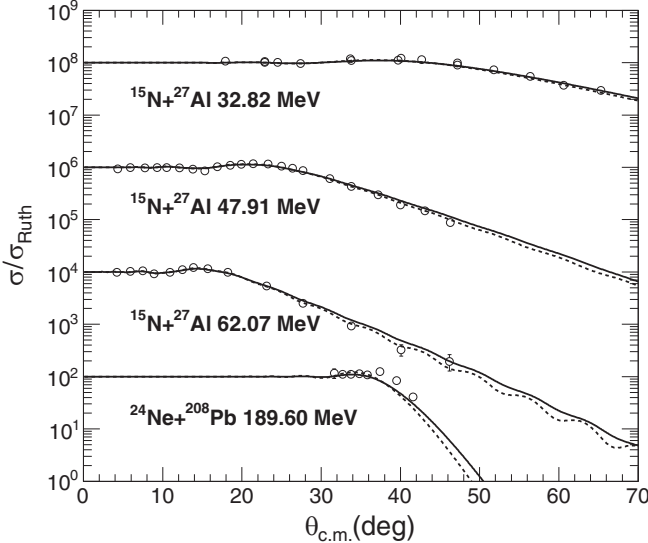


FIG. 12. Same as Fig. 9, but for ^{15}N and ^{24}Ne projectiles. The experimental data are from Refs. [72,73].

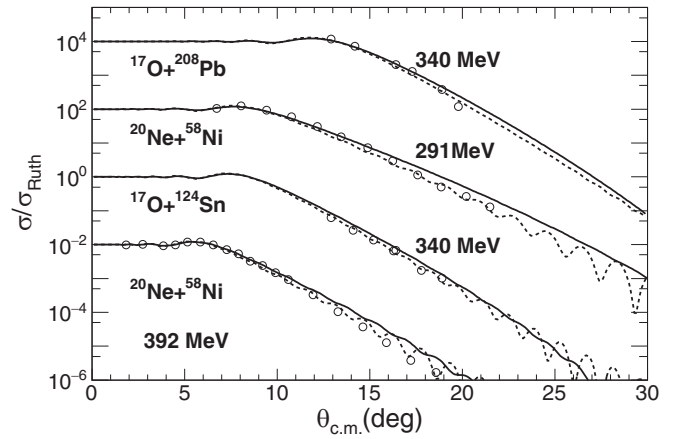


FIG. 13. Same as Fig. 9, but for ^{17}O and ^{20}Ne projectiles. The experimental data are from Refs. [74–76].

butions. Q^2 values were calculated for each parameter set. The results are shown in Figs. 2(a) and 2(d). It is interesting to see that the slope and the intercept parameters of the real potential anticorrelate with each other. This may be understood by the fact that changes in the slope parameter can, to some extent, be compensated by changes in the intercept parameter without deteriorating the description of the experimental data. Those of the imaginary part seem also

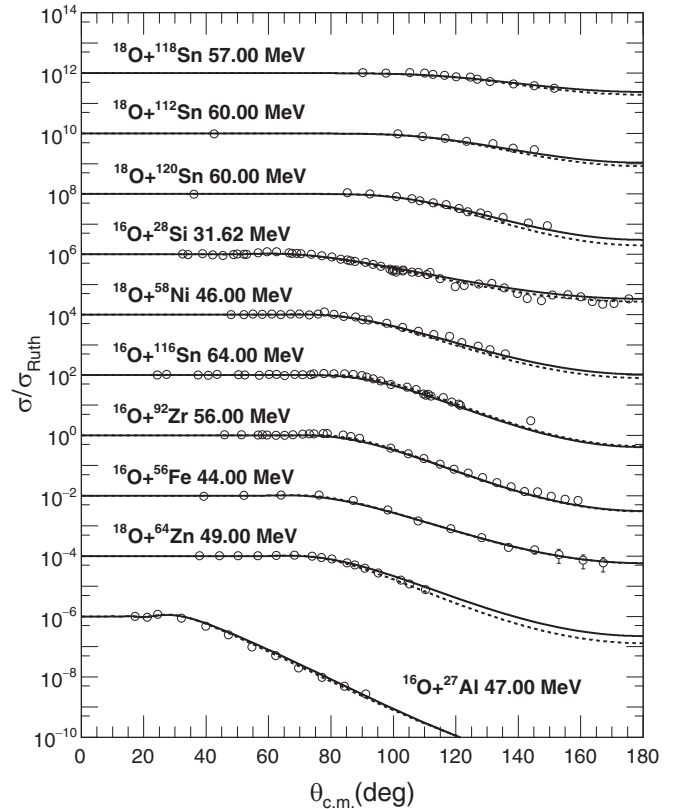


FIG. 14. Same as Fig. 9, but for ^{16}O and ^{18}O projectiles. The experimental data are from Refs. [77–84].

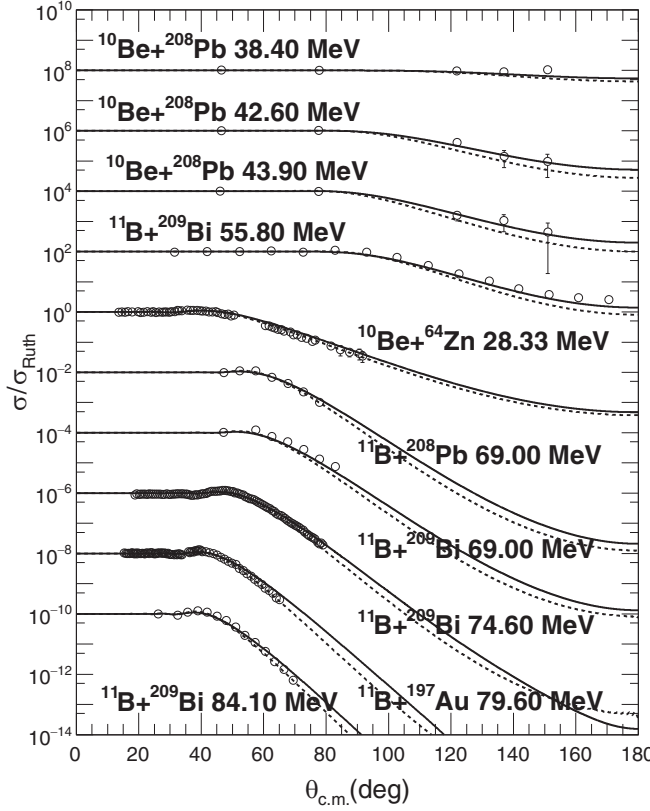


FIG. 15. Same as Fig. 9, but for ^{10}Be and ^{11}B projectiles. The experimental data are from Refs. [85–90].

anticorrelated, but these two parameters, t_i and k_i , are much more scattered than the two of the real part. This suggests, again, that the elastic-scattering cross sections cannot well constrain the optical model potential parameters at low energies and this problem is more serious in the imaginary part than in the real part. Such broad distributions of the $t_{r,i}$ and $k_{r,i}$ values coincide with the scattered optimum N_r and N_i values obtained with the separate fitting method in Figs. 1(a) and 1(b).

The values of $\{t_r, k_r, t_i, k_i\}$, which result in the minimum Q^2 value, are listed in Table I as the SMF method. The corresponding linear functions of $N_r(E_{\text{lab}})$ and $N_i(E_{\text{lab}})$ are displayed in Fig. 3. Since no obvious discrete potential families are observed, it seems reasonable to perform a statistical analysis on the results in Figs. 2(a) and 2(d) for a global potential parameter set from this SMF method. The distributions of $t_{r,i}$ and $k_{r,i}$ values are fitted with Gaussian functions for $1/Q^2 \geq 0.01$ (this choice is rather arbitrary but the results do not change much if another criteria is used). Since the $\{t_r, k_r, t_i, k_i\}$ values obtained in this way are the averaged results of the simultaneous fitting (ASMF), we designate them as the ASMF results. As one can see, their values are very close to the ones of the SMF method. These values are also listed in Table I, together with those from the SPF and SMF methods.

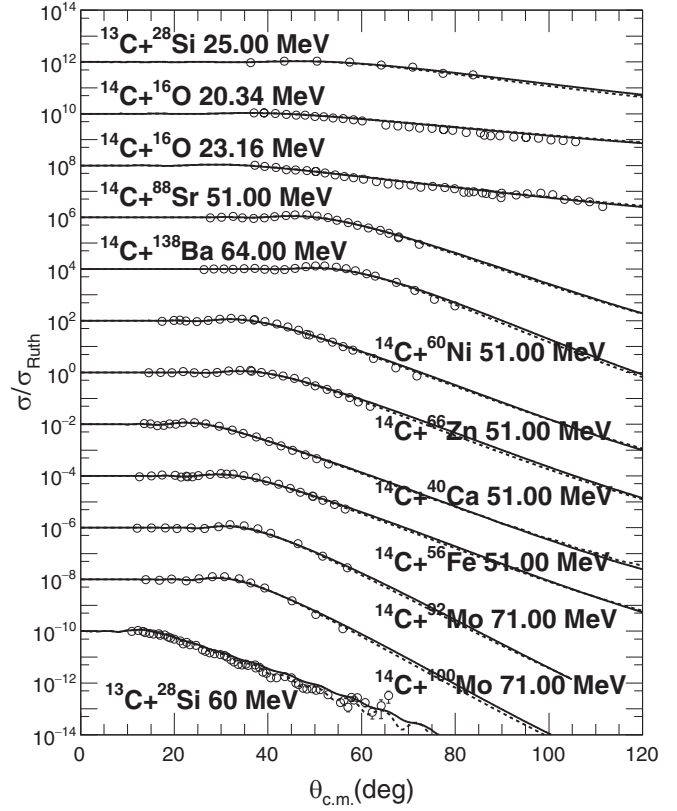


FIG. 16. Same as Fig. 9, but for $^{13,14}\text{C}$ projectiles. The experimental data are from Refs. [91–96].

C. Combination with the systematics of Ref. [12]

The slope parameters obtained in this work, which are based on experimental data of relatively low energies, are different from those reported in Ref. [12] for higher incident energies. Since the latter has been seen to be rather successful in describing heavy-ion elastic scattering [13–16], it will be useful to combine it with the current systematics, which is confined with the experimental data mainly at the low-energy region. The result is given in Eqs. (8) and (9), which are smooth connections between the results obtained in this work and those in Ref. [12]:

$$N_r = \frac{b_r(x - x_0^r) + \sqrt{c_r(x - x_0^r)^2 + d_r}}{2a_r} + y_0^r, \quad (8)$$

$$N_i = \frac{b_i(x - x_0^i) + \sqrt{c_i(x - x_0^i)^2 + d_i}}{2a_i} + y_0^i. \quad (9)$$

The parameters $b_{r,i}$, $a_{r,i}$, $x_0^{r,i}$, $c_{r,i}$, $d_{r,i}$, and $y_0^{r,i}$ are listed in Table I for the three fitting methods. The combined systematic parameters are depicted in Fig. 3. As one can see, these are three hyperbolic functions by taking the two lines of different slopes as asymptotes, where the asymptotes before the intersection points are extracted from the three fitting methods described previously, while the one after the intersection points are the results of Ref. [12]. From Figs. 3(a) and 3(b), it is seen that the combined renormalization factors of the real potential for all three methods decrease with increasing

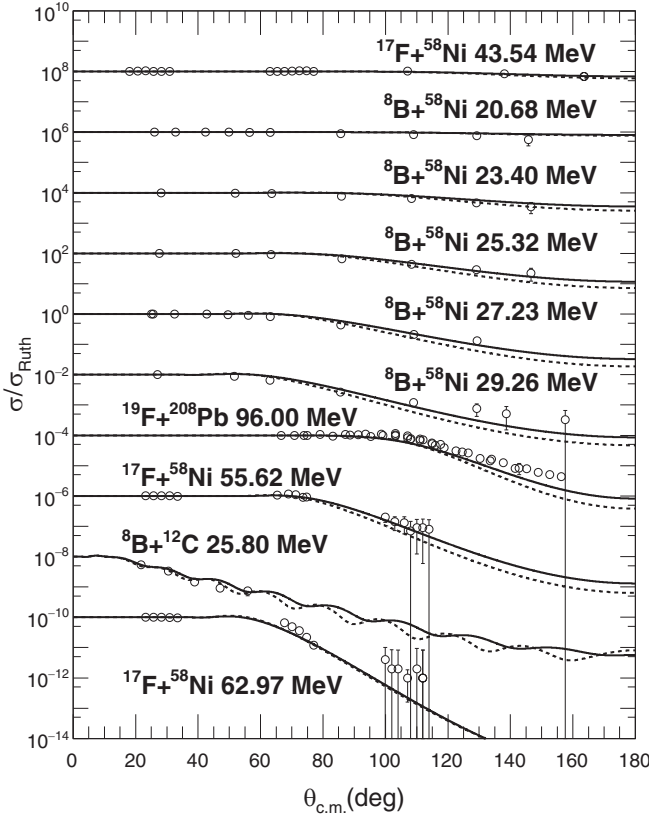


FIG. 17. Same as Fig. 9, but for ${}^8\text{B}$, ${}^{17}\text{F}$, and ${}^{19}\text{F}$ projectiles at low energies. The experimental data are from Refs. [97–100].

incident energy and rise slowly after the energy determined by the intersection points, while the ones of the imaginary potential decrease with the incident energy and become constant when E_{lab}/A_p is larger than around 20 MeV.

The overall agreement between the theoretical calculations and the experimental data is fairly good, as can be seen from the Q^2 values listed in Table II calculated with the new energy-dependent potential parameters derived from present

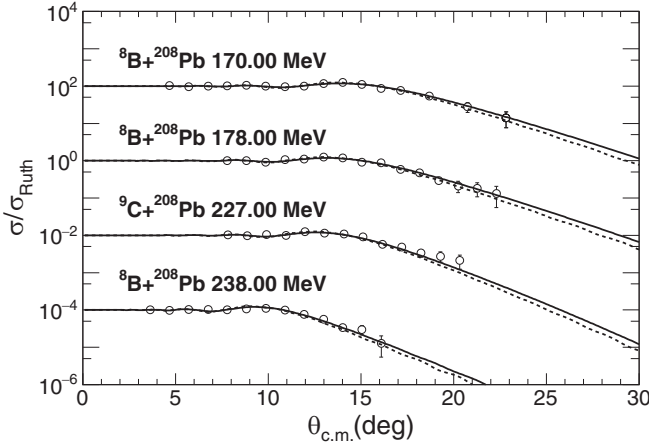


FIG. 18. Same as Fig. 9, but for ${}^8\text{B}$ and ${}^9\text{C}$ projectiles at high energies. The experimental data are from Refs. [15,16,101].

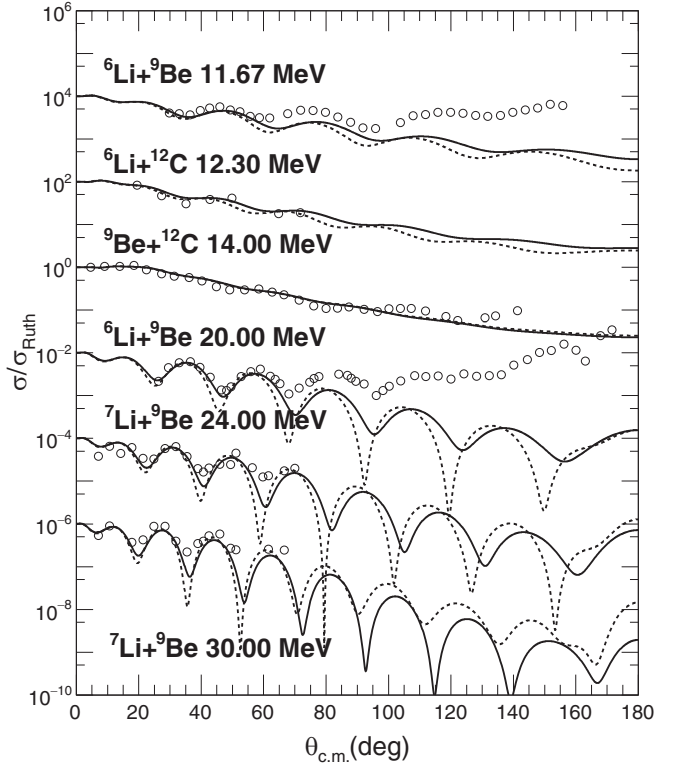


FIG. 19. Comparisons between optical model calculations and experimental data for ${}^6\text{Li}$, ${}^7\text{Li}$, and ${}^9\text{Be}$ from light targets at incident energies indicated in the figure. The experimental data are from Refs. [37,100,102,103].

work [Eqs. (8) and (9)] for the three search strategies by taking $N = 1$ in Eq. (7). After further examinations with both weakly and tightly bound nuclei, it was found that the systematic parameters given by the ASMF method provide a better average description of the overall trend of the interaction as a function of energy and become a reasonable option for reliable interpolations at the energies needed when the corresponding data are not available.

D. Verification of the new systematic potential

1. Elastic scattering of ${}^9\text{Be}$

In order to examine the prediction power and the range of applicability of the new systematic potential, extensive comparisons between the experimental data and results of optical model calculations are made. The results are shown for ${}^9\text{Be}$ elastic scattering from light mass targets ${}^{16}\text{O}$, ${}^{27}\text{Al}$, and ${}^{28}\text{Si}$ in Fig. 4, from medium mass targets ${}^{64}\text{Zn}$, ${}^{80}\text{Se}$, and ${}^{89}\text{Y}$ in Fig. 5, and from heavy targets ${}^{120}\text{Sn}$, ${}^{144}\text{Sm}$, ${}^{197}\text{Au}$, ${}^{208}\text{Pb}$, and ${}^{209}\text{Bi}$ in Figs. 6 and 7. Comparisons are also made with the theoretical results using the São Paulo potential of version 2 (SPP2). These results demonstrate that the new systematic potential presented in this work accounts well for the elastic scattering of ${}^9\text{Be}$ from various targets from light-heavy to heavy nuclei at low energies down to the vicinity of the Coulomb barriers. This combined systematic potential remains good in describing the elastic scattering at incident

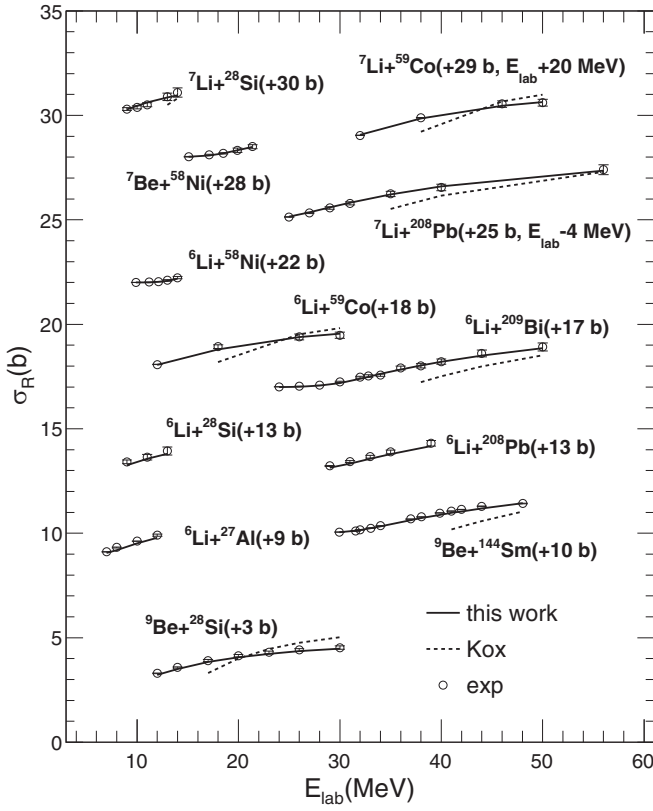


FIG. 20. Comparisons between optical model calculations and experimental data for total-reaction cross sections of ${}^6\text{Li}$, ${}^7\text{Li}$, ${}^7\text{Be}$, and ${}^9\text{Be}$ with targets indicated in the figure at various incident energies. The data sets are offset for optimum view. The experimental data are from Refs. [47,48,98,104–109].

energies well above the Coulomb barrier, which is demonstrated in Fig. 8, where theoretical calculations are compared with experimental data of ${}^9\text{Be}$ elastic scattering from various targets at incident energies more than 4 times the Coulomb barriers.

2. Examination with other projectiles

Although obtained from analyses of ${}^6,7\text{Li}$ elastic-scattering data, the systematic potential of Ref. [12] is found to account for the elastic-scattering and total-reaction cross-section data of many other nuclei. We examine the applicability of this new systematic potential to projectiles other than ${}^9\text{Be}$ as well, focusing on the low-energy region. The results are shown in Fig. 9 for ${}^6\text{Li}$, Fig. 10 for ${}^7\text{Li}$, Fig. 11 for ${}^{14}\text{N}$, Fig. 12 for ${}^{15}\text{N}$ and ${}^{24}\text{Ne}$, Fig. 13 for ${}^{17}\text{O}$ and ${}^{20}\text{Ne}$, Fig. 14 for ${}^{16}\text{O}$ and ${}^{18}\text{O}$, Fig. 15 for ${}^{10}\text{Be}$ and ${}^{11}\text{B}$, and Fig. 16 for ${}^{13}\text{C}$ and ${}^{14}\text{C}$. They all show that the new systematic potential describes the elastic-scattering angular distributions reasonably well.

The present systematic potential is also observed to be applicable for weakly bound nuclei. Figures 17 and 18 depict the comparisons between the experimental elastic-scattering cross sections of ${}^8\text{B}$, ${}^9\text{C}$, and ${}^{17,19}\text{F}$ and theoretical calculations with the present systematic potential for incident energies between 2 and 30 MeV/nucleon.

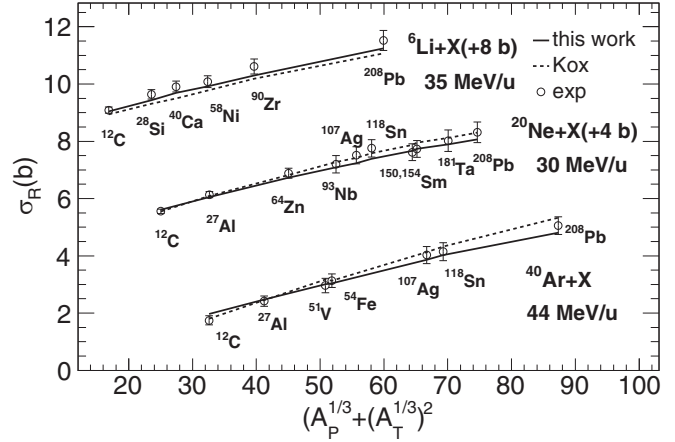


FIG. 21. Comparisons between optical model calculations and experimental data for total-reaction cross sections of ${}^6\text{Li}$, ${}^{20}\text{Ne}$, and ${}^{40}\text{Ar}$ with various targets. The experimental data are from Refs. [110–112]. The solid and dotted curves are results of the present work and of the Kox formula, respectively.

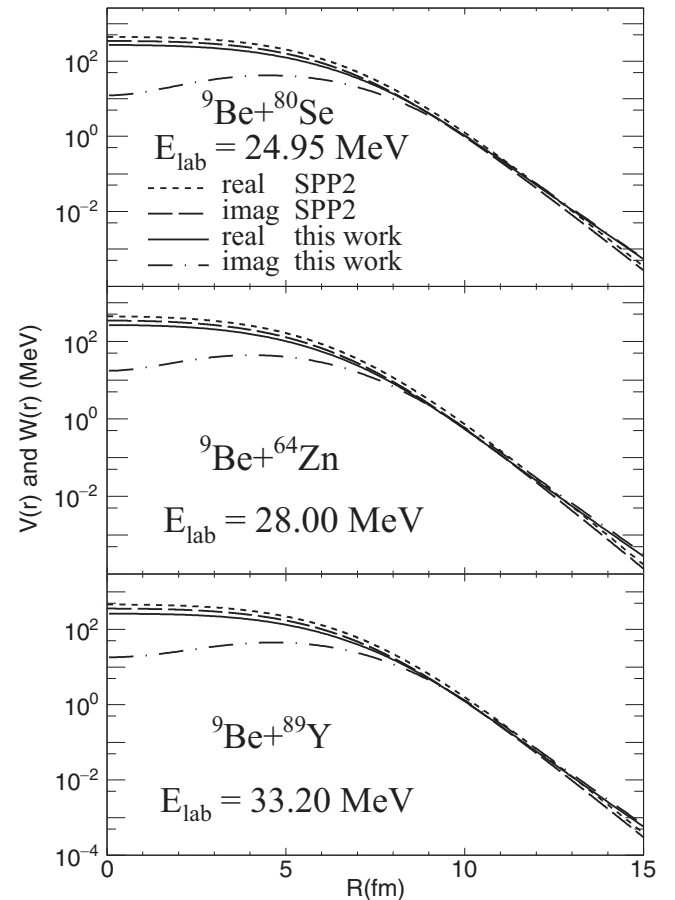


FIG. 22. Real and imaginary parts of the potentials calculated with the current systematic potential and those of SPP2 for ${}^9\text{Be}$ scattering by ${}^{64}\text{Zn}$, ${}^{80}\text{Se}$, and ${}^{89}\text{Y}$ at $E_{\text{lab}} = 28$, 24.95, and 33.2 MeV, respectively. Note that these potentials are displayed in the logarithmic scale to make the potential depths around the nuclear surface region visible.

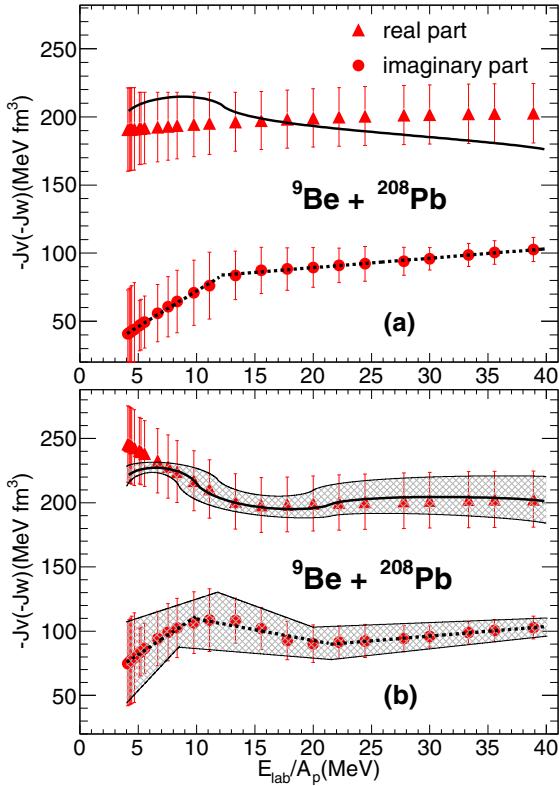


FIG. 23. Volume integrals per nucleon pair calculated with (a) the potential of Ref. [12] and (b) the current systematic potential for the ${}^9\text{Be} + {}^{208}\text{Pb}$ system as a function of the incident energy. The dashed curves show the energy intervals chosen to calculate ΔJ_v in Eq. (13) whose results are shown by the solid curves. See text for details.

The present systematic potential is established with experimental data of intermediate-mass and heavy targets. Experimental data with light targets are not included in the process of data fitting. It is interesting to see how this new systematic potential works when it is extrapolated to light-mass target regions. In Fig. 19, we show results of calculations with our new systematic potential and their comparisons with the experimental data for ${}^6,7\text{Li}$ and ${}^9\text{Be}$ elastic scattering from ${}^9\text{Be}$ and ${}^{12}\text{C}$ targets. Although the comparison with experimental data with light targets is not as good as the comparisons with heavy- or intermediate-mass targets, the degree of agreement is still reasonable. The optical model calculations could not reproduce the increase of the cross sections at backward angles for the ${}^6\text{Li} + {}^9\text{Be}$ cases at 11.67 and 20 MeV. This is expected because, as reported in Ref. [102], the t -transfer and compound reaction mechanisms contribute considerably at these angles and they are not supposed to be accounted for by optical model calculations.

3. Total reaction cross sections

Besides the elastic-scattering angular distributions, total-reaction cross sections (σ_R) are also important quantities to examine the systematic optical model potentials. We did not confine the potential parameters with total-reaction cross sec-

tions in the present work. So comparisons with total-reaction cross sections can be served to further verify our new systematic potential. The comparisons are made for ${}^6,7\text{Li}$ and ${}^7,9\text{Be}$ projectiles on targets ${}^{27}\text{Al}$, ${}^{28}\text{Si}$, and ${}^{58}\text{Ni}$ in Fig. 20 at low energies and for ${}^6\text{Li}$, ${}^{20}\text{Ne}$, and ${}^{40}\text{Ar}$ on various targets at relatively high energies around 35 MeV/nucleon in Fig. 21. Very good agreement between theoretical calculations and experimental data is found for these systems. Especially, the calculations of σ_R reproduce rather well experimental data at the low-energy region. The theoretical values are also close to those obtained by Kox's formula [110,113].

IV. DISCUSSIONS

A. Similar description of experimental data with different systematic potentials

The comparisons between results of optical model calculations with the present systematic potential and with those of SPP2 are, in general, rather satisfactory. Both systematic potentials are capable of describing the experimental data reasonably well. For instance, in Fig. 5, the two systematic potentials describe the ${}^9\text{Be} + {}^{64}\text{Zn}$, ${}^9\text{Be} + {}^{80}\text{Se}$, and ${}^9\text{Be} + {}^{89}\text{Y}$ elastic scattering at $E_{\text{lab}} = 28$, 24.95, and 33.2 MeV nearly equally well. The corresponding total-reaction cross sections are also very close, which are, respectively, 1083, 739, and 1162 mb with the present potential and 1090, 724, and 1151 mb with SPP2. Their corresponding potentials are, however, rather different, as shown in Fig. 22. Large differences in both the strengths and the radial shapes are seen in these potentials, especially in the inner regions. The real and imaginary parts of the present potentials are much shallower than those of SPP2. Another thing worth mentioning is that the real and imaginary parts of the present potentials are different in both depth and radial shape, but those of the SPP2 parts have the same radial shapes and their depths differ by a factor of 0.78. This suggests that the elastic-scattering and total-reaction data cannot provide sufficient constraint to the inner part of the heavy-ion optical model potentials. This might be one of the reasons why sometimes quite different potentials produce very similar angular distributions of heavy-ion elastic scattering. It should be noted that this problem even exists at much higher energies, for instance, the ${}^{16}\text{O} + {}^{16}\text{O}$ system at 70 MeV/nucleon studied in Ref. [8].

B. Examination with the dispersion relation

According to the theory of the dispersion relation, the real part of the optical model potential can be divided into two terms [114]:

$$V(r; E) = V_0(r; E) + \Delta V(r; E), \quad (10)$$

where $V_0(r; E)$ is energy independent or at most depends slowly and smoothly on the incident energy E . Therefore, the energy dependence of the real potential mainly comes from the $\Delta V(r; E)$ term, which is related with the imaginary part of the OMP [$W(r; E)$] via the dispersion relation

$$\Delta V(r; E) = \frac{P}{\pi} \int_0^\infty \frac{W(r; E')}{E' - E} dE', \quad (11)$$

where P stands for principal value. Systematic potentials, whose energy dependence are confined with experimental data, allow one to examine the dispersion relations between their real and imaginary parts. From another point of view, a systematic potential could be assessed by checking if its real and imaginary parts satisfy the dispersion relation.

Practically, it is profitable to study the dispersion relations between the volume integrals of the real and imaginary potentials. In doing so, the dispersion relation in Eq. (11) takes the following form:

$$J_v(E) = J_{v,0}(E) + \Delta J_v \equiv J_{v,0} + \frac{P}{\pi} \int \frac{J_w(E')}{E' - E} dE', \quad (12)$$

where $J_{v,0}(E)$ is assumed to be a constant or depends slowly and smoothly on E (we take it to be a constant in this work), and J_v and J_w are the volume integrals per interacting nucleon pair of real and imaginary parts, respectively.

To give an analytic form of the dispersion relation, we used the linear schematic model of the energy dependence of the imaginary potential as proposed in Ref. [114], where $J_w(E)$ is separated into a series of linear segments. The contribution from each segment to the total dispersion is

$$\Delta J_v^{ij}(E) = (J_w^{ij}/\pi)[\xi_i \ln|\xi_i| - \xi_j \ln|\xi_j|], \quad (13)$$

where $J_w^{ij} = J_w(E_i) - J_w(E_j)$, $\xi_i = (E - E_i)/\Delta_{ij}$, $\xi_j = (E - E_j)/\Delta_{ij}$, $\Delta_{ij} = E_j - E_i > 0$, and E_i and E_j are the boundaries of the energy intervals.

The dispersion relation is checked for the ${}^9\text{Be} + {}^{208}\text{Pb}$ system with the present updated potential and the original systematic potential in Ref. [12]. The results are shown in Fig. 23. Clearly, with the updated systematic potential, the dispersion relation between the real and the imaginary potentials is much better fulfilled than with the original potential, which was obtained mainly from analysis of the experimental data that are well above the Coulomb barriers. The energy dependence of the real part of the present new systematic potential is consistent with the prediction of the dispersion relation within nearly the whole energy range except at low energies, which are below about 5 MeV/nucleon, where the

potentials have the biggest uncertainties. The uncertainties of the J_v and J_w values in each energy interval were determined in the following way: within each energy interval, three sets of experimental data were used to find their Q^2 values as functions of N_r and N_i . The uncertainties of N_r and N_i in those intervals, ΔN_r and ΔN_i , respectively, were chosen so that the Q^2 values associated with $N_r \pm \Delta N_r$ and $N_i \pm \Delta N_i$ were larger than their corresponding minimum Q^2 values by a factor of 1.8. The uncertainties of J_v and J_w were then determined by these ΔN_r and ΔN_i values.

V. SUMMARY

In this work, we extend the systematic nucleus-nucleus potential proposed in Ref. [12], which was obtained by analyzing ${}^6\text{Li}$ and ${}^7\text{Li}$ elastic-scattering data with the range of incident energies between around 10 to 100 MeV/nucleon, to lower energies. This is realized by analyzing the elastic-scattering angular distributions of the ${}^9\text{Be}$ projectile on various targets with mass numbers ranging from 16 to 209 at incident energies from 12 to 202 MeV and combining the energy dependence of the potential established in this low-energy region with that of Ref. [12]. This updated systematic nucleus-nucleus potential now covers a range of incident energies from around half of the Coulomb barrier to around 100 MeV/nucleon. Good agreement was found between results of optical model calculations with this new potential and the experimental data of both stable and unstable nuclei for elastic-scattering and total-reaction cross sections. With such improved description of the nucleus-nucleus interactions at low energies, great improvement is also found in the degree of agreement between the energy dependence of the real part of this updated systematic potential and the prediction of the dispersion relation.

ACKNOWLEDGMENTS

This work was financially supported by the National Natural Science Foundation of China (Grants No. U2067205, No. 12105330, and No. 12122511) and the Youth Innovation Promotion Association CAS (Grant No. 2020411).

-
- [1] D. Y. Pang, Y. L. Ye, and F. R. Xu, *J. Phys. G: Nucl. Part. Phys.* **39**, 095101 (2012).
 - [2] D. Y. Pang, P. Roussel-Chomaz, H. Savajols, R. L. Varner, and R. Wolski, *Phys. Rev. C* **79**, 024615 (2009).
 - [3] X. Li, C. Liang, and C. Cai, *Nucl. Phys. A* **789**, 103 (2007).
 - [4] D. Y. Pang, Y. L. Ye, and F. R. Xu, *Phys. Rev. C* **83**, 064619 (2011).
 - [5] L. C. Chamon, B. V. Carlson, L. R. Gasques, D. Pereira, C. De Conti, M. A. G. Alvarez, M. S. Hussein, M. A. Cândido Ribeiro, E. S. Rossi, Jr., and C. P. Silva, *Phys. Rev. C* **66**, 014610 (2002).
 - [6] M. A. Cândido Ribeiro, L. C. Chamon, D. Pereira, M. S. Hussein, and D. Galetti, *Phys. Rev. Lett.* **78**, 3270 (1997).
 - [7] L. C. Chamon, D. Pereira, M. S. Hussein, M. A. Cândido Ribeiro, and D. Galetti, *Phys. Rev. Lett.* **79**, 5218 (1997).
 - [8] T. Furumoto, W. Horiuchi, M. Takashina, Y. Yamamoto, and Y. Sakuragi, *Phys. Rev. C* **85**, 044607 (2012).
 - [9] Y. Xu, Y. Han, J. Hu, H. Liang, Z. Wu, H. Guo, and C. Cai, *Phys. Rev. C* **97**, 014615 (2018).
 - [10] Y. Xu, Y. Han, H. Liang, Z. Wu, H. Guo, and C. Cai, *Phys. Rev. C* **99**, 034618 (2019).
 - [11] Y. Xu, Y. Han, H. Liang, Z. Wu, H. Guo, and C. Cai, *Chin. Phys. C* **44**, 034101 (2020).
 - [12] Y. P. Xu and D. Y. Pang, *Phys. Rev. C* **87**, 044605 (2013).
 - [13] F. Duan, Y. Yang, K. Wang, A. Moro, V. Guimarães, D. Pang, J. Wang, Z. Sun, J. Lei, A. Di Pietro, X. Liu, G. Yang, J. Ma, P. Ma, S. Xu, Z. Bai, X. Sun, Q. Hu, J. Lou, X. Xu *et al.*, *Phys. Lett. B* **811**, 135942 (2020).
 - [14] Y. Y. Yang, J. S. Wang, Q. Wang, D. Y. Pang, J. B. Ma, M. R. Huang, P. Ma, S. L. Jin, J. L. Han, Z. Bai, L. Jin, J. B. Chen,

- Q. Hu, R. Wada, S. Mukherjee, Z. Y. Sun, R. F. Chen, X. Y. Zhang, Z. G. Hu, X. H. Yuan *et al.*, *Phys. Rev. C* **90**, 014606 (2014).
- [15] Y. Y. Yang, J. S. Wang, Q. Wang, D. Pang, J. B. Ma, M. R. Huang, J. L. Han, P. Ma, S. L. Jin, Z. Bai, Q. Hu, L. Jin, J. B. Chen, N. Keeley, K. Rusek, R. Wada, S. Mukherjee, Z. Y. Sun, R. F. Chen, X. Y. Zhang *et al.*, *Phys. Rev. C* **87**, 044613 (2013).
- [16] Y. Y. Yang, X. Liu, D. Y. Pang, D. Patel, R. F. Chen, J. S. Wang, P. Ma, J. B. Ma, S. L. Jin, Z. Bai, V. Guimarães, Q. Wang, W. H. Ma, F. F. Duan, Z. H. Gao, Y. C. Yu, Z. Y. Sun, Z. G. Hu, S. W. Xu, S. T. Wang *et al.*, *Phys. Rev. C* **98**, 044608 (2018).
- [17] E. Bauge, J. P. Delaroche, and M. Girod, *Phys. Rev. C* **58**, 1118 (1998).
- [18] E. Bauge, J. P. Delaroche, and M. Girod, *Phys. Rev. C* **63**, 024607 (2001).
- [19] D. Perkin, A. Kobos, and J. Rook, *Nucl. Phys. A* **245**, 343 (1975).
- [20] F. Petrovich, D. Stanley, L. A. Parks, and P. Nagel, *Phys. Rev. C* **17**, 1642 (1978).
- [21] N. Keeley, K. W. Kemper, and K. Rusek, *Phys. Rev. C* **64**, 031602(R) (2001).
- [22] V. V. Parkar, V. Jha, S. K. Pandit, S. Santra, and S. Kailas, *Phys. Rev. C* **87**, 034602 (2013).
- [23] P. Descouvemont and N. Itagaki, *Phys. Rev. C* **97**, 014612 (2018).
- [24] A. Arazi, J. Casal, M. Rodríguez-Gallardo, J. M. Arias, R. Lichtenthaler Filho, D. Abriola, O. A. Capurro, M. A. Cardona, P. F. F. Carnelli, E. de Barbará, J. Fernández Niello, J. M. Figueira, L. Fimiani, D. Hojman, G. V. Martí, D. Martínez Heimman, and A. J. Pacheco, *Phys. Rev. C* **97**, 044609 (2018).
- [25] J. Casal, M. Rodríguez-Gallardo, and J. M. Arias, *Phys. Rev. C* **92**, 054611 (2015).
- [26] P. Descouvemont, T. Druet, L. F. Canto, and M. S. Hussein, *Phys. Rev. C* **91**, 024606 (2015).
- [27] S. K. Pandit, V. Jha, K. Mahata, S. Santra, C. S. Palshetkar, K. Ramachandran, V. V. Parkar, A. Shrivastava, H. Kumawat, B. J. Roy, A. Chatterjee, and S. Kailas, *Phys. Rev. C* **84**, 031601(R) (2011).
- [28] N. Keeley, N. Alamanos, K. Rusek, and K. W. Kemper, *Phys. Rev. C* **71**, 014611 (2005).
- [29] Y. Sakuragi, *Phys. Rev. C* **35**, 2161 (1987).
- [30] Y. Hirabayashi, S. Okabe, and Y. Sakuragi, *Phys. Lett. B* **221**, 227 (1989).
- [31] Y. Hirabayashi and Y. Sakuragi, *Phys. Lett. B* **258**, 11 (1991).
- [32] Experimental nuclear reaction data, <https://www.nndc.bnl.gov/exfor/exfor.htm>.
- [33] Nuclear reaction video, http://nrv.jinr.ru/nrv/webnrv/elastic_scattering/reactions.php.
- [34] J. Eck, T. Ophel, P. Clark, and D. Weisser, *Nucl. Phys. A* **334**, 519 (1980).
- [35] N. Yu, H. Q. Zhang, H. M. Jia, S. T. Zhang, M. Ruan, F. Yang, Z. D. Wu, X. X. Xu, and C. L. Bai, *J. Phys. G: Nucl. Part. Phys.* **37**, 075108 (2010).
- [36] R. Varner, W. Thompson, T. McAbee, E. Ludwig, and T. Clegg, *Phys. Rep.* **201**, 57 (1991).
- [37] E. Ungricht, D. Balzer, M. Hugi, J. Lang, R. Müller, L. Jarczyk, B. Kamys, and A. Strzalkowski, *Nucl. Phys. A* **313**, 376 (1979).
- [38] Y. A. Glukhov, A. A. Ogloblin, K. P. Artemov, and V. P. Rudakov, *Phys. At. Nucl.* **73**, 14 (2010).
- [39] C. Fulmer, G. Satchler, K. Erb, D. Hensley, R. Auble, J. Ball, F. Bertrand, and E. Gross, *Nucl. Phys. A* **427**, 545 (1984).
- [40] P. R. S. Gomes, R. M. Anjos, C. Muri, J. Lubian, I. Padron, L. C. Chamón, R. Liguori Neto, N. Added, J. O. Fernández Niello, G. V. Martí, O. A. Capurro, A. J. Pacheco, J. E. Testoni, and D. Abriola, *Phys. Rev. C* **70**, 054605 (2004).
- [41] R. Anjos, C. Muri, J. Lubian, P. Gomes, I. Padron, J. Alves, G. Martí, J. Fernández Niello, A. Pacheco, O. Capurro, D. Abriola, J. Testoni, M. Ramírez, R. Liguori Neto, and N. Added, *Phys. Lett. B* **534**, 45 (2002).
- [42] M. S. Zisman, J. G. Cramer, D. A. Goldberg, J. W. Watson, and R. M. DeVries, *Phys. Rev. C* **21**, 2398 (1980).
- [43] M. Hugi, J. Lang, R. Müller, E. Ungricht, K. Bodek, L. Jarczyk, B. Kamys, A. Magiera, A. Strzalkowski, and G. Willim, *Nucl. Phys. A* **368**, 173 (1981).
- [44] S. B. Moraes, P. R. S. Gomes, J. Lubian, J. J. S. Alves, R. M. Anjos, M. M. Sant'Anna, I. Padrón, C. Muri, R. Liguori Neto, and N. Added, *Phys. Rev. C* **61**, 064608 (2000).
- [45] V. Scuderi, A. Di Pietro, L. Acosta, F. Amorini, M. J. G. Borge, P. Figuera, M. Fisichella, L. M. Fraile, J. Gómez-Camacho, H. Jeppesen, M. Lattuada, I. Martel, M. Milin, A. Musumarra, M. Papa, M. G. Pellegriti, R. Raabe, G. Randisi, F. Rizzo, D. Santonocito *et al.*, *AIP Conf. Proc.* **1231**, 191 (2010).
- [46] F. Gollan, D. Abriola, A. Arazi, O. Capurro, M. Cardona, E. de Barbará, D. Hojman, G. Martí, A. Pacheco, D. Rodrigues, and J. Testoni, *Nucl. Phys. A* **979**, 87 (2018).
- [47] P. Gomes, J. Lubian, B. Paes, V. Garcia, D. Monteiro, I. Padrón, J. Figueira, A. Arazi, O. Capurro, L. Fimiani, A. Negri, G. Martí, J. Fernández Niello, A. Gómez-Camacho, and L. Canto, *Nucl. Phys. A* **828**, 233 (2009).
- [48] P. R. S. Gomes, I. Padron, E. Crema, O. A. Capurro, J. O. Fernández Niello, A. Arazi, G. V. Martí, J. Lubian, M. Trotta, A. J. Pacheco, J. E. Testoni, M. D. Rodríguez, M. E. Ortega, L. C. Chamón, R. M. Anjos, R. Veiga, M. Dasgupta, D. J. Hinde, and K. Hagino, *Phys. Rev. C* **73**, 064606 (2006).
- [49] F. Gollan, D. Abriola, A. Arazi, M. Cardona, E. de Barbará, D. Hojman, R. Id Betan, G. Martí, A. Pacheco, D. Rodrigues, and M. Tognari, *Nucl. Phys. A* **1000**, 121789 (2020).
- [50] R. J. Woolliscroft, B. R. Fulton, R. L. Cowin, M. Dasgupta, D. J. Hinde, C. R. Morton, and A. C. Berriman, *Phys. Rev. C* **69**, 044612 (2004).
- [51] F. F. Duan, Y. Y. Yang, D. Y. Pang, B. T. Hu, J. S. Wang, K. Wang, G. Yang, V. Guimarães, P. Ma, S. W. Xu, X. Q. Liu, J. B. Ma, Z. Bai, Q. Hu, S. Y. Jin, X. X. Sun, J. S. Yao, H. K. Qi, and Z. Y. Sun, *Chin. Phys. C* **44**, 024001 (2020).
- [52] C. Signorini, A. Andriguetto, J. Guo, M. Ruan, L. Stroe, F. Soramel, K. Löbner, L. Müller, D. Pierroutsakou, M. Romoli, K. Rudolph, I. Thompson, M. Trotta, and A. Vitturi, *Nucl. Phys. A* **701**, 23 (2002).
- [53] C. S. Palshetkar, S. Santra, A. Shrivastava, A. Chatterjee, S. K. Pandit, K. Ramachandran, V. V. Parkar, V. Nanal, V. Jha, B. J. Roy, and S. Kalais, *Phys. Rev. C* **89**, 064610 (2014).
- [54] M. Zadro, P. Figuera, A. Di Pietro, F. Amorini, M. Fisichella, O. Goryunov, M. Lattuada, C. Maiolino, A. Musumarra, V. Ostashko, M. Papa, M. G. Pellegriti, F. Rizzo, D. Santonocito, V. Scuderi, and D. Torresi, *Phys. Rev. C* **80**, 064610 (2009).
- [55] A. Pakou, N. Alamanos, A. Lagoyannis, A. Gillibert, E. Pollacco, P. Assimakopoulos, G. Doukelis, K. Ioannides, D. Karadimos, D. Karamanis, M. Kokkoris, E. Kossionides,

- N. Nicolis, C. Papachristodoulou, N. Patronis, G. Perdikakis, and D. Pierroutsakou, *Phys. Lett. B* **556**, 21 (2003).
- [56] N. Keeley, J. M. Cook, K. W. Kemper, B. T. Roeder, W. D. Weintraub, F. Maréchal, and K. Rusek, *Phys. Rev. C* **68**, 054601 (2003).
- [57] J. M. Figueira, J. O. Fernandez Niello, A. Arazi, O. A. Capurro, P. Carnelli, L. Fimiani, G. V. Martí, D. M. Heimann, A. E. Negri, A. J. Pacheco, J. Lubian, D. S. Monteiro, and P. R. S. Gomes, *Phys. Rev. C* **81**, 024613 (2010).
- [58] L. T. Chua, F. D. Becchetti, J. Jänecke, and F. L. Milder, *Nucl. Phys. A* **273**, 243 (1976).
- [59] K. D. Veal, C. R. Brune, W. H. Geist, H. J. Karwowski, E. J. Ludwig, E. E. Bartosz, P. D. Cathers, T. L. Drummer, K. W. Kemper, A. M. Eiró, F. D. Santos, B. Kozlowska, H. J. Maier, and I. J. Thompson, *Phys. Rev. C* **60**, 064003 (1999).
- [60] R. Wadsworth, M. D. Cohler, M. J. Smithson, D. L. Watson, F. Jundt, L. Kraus, I. Linck, and J. C. Sens, *J. Phys. G: Nucl. Phys.* **9**, 1237 (1983).
- [61] P. Schwandt, W. W. Jacobs, M. D. Kaitchuck, P. P. Singh, W. D. Plough, F. D. Becchetti, and J. Jänecke, *Phys. Rev. C* **24**, 1522 (1981).
- [62] X. Chen, Y.-W. Lui, H. L. Clark, Y. Tokimoto, and D. H. Youngblood, *Phys. Rev. C* **76**, 054606 (2007).
- [63] L. Yang, C. J. Lin, H. M. Jia, F. Yang, Z. D. Wu, X. X. Xu, H. Q. Zhang, Z. H. Liu, P. F. Bao, L. J. Sun, and N. R. Ma, *Phys. Rev. C* **89**, 044615 (2014).
- [64] A. Zeller, D. Weisser, T. Ophel, and D. Hebbard, *Nucl. Phys. A* **332**, 515 (1979).
- [65] H. Freiesleben, G. T. Rizzo, and J. R. Huizenga, *Phys. Rev. C* **12**, 42 (1975).
- [66] C. Glover, R. Cutler, and K. Kemper, *Nucl. Phys. A* **341**, 137 (1980).
- [67] A. Zeller, K. Kemper, T. Ophel, D. Weisser, D. Hebbard, A. Johnston, and G. Hickey, *Nucl. Phys. A* **309**, 255 (1978).
- [68] M. E. Williams, R. H. Davis, C. I. Delaune, G. M. Hudson, K. W. Kemper, and A. F. Zeller, *Phys. Rev. C* **11**, 906 (1975).
- [69] J. Mateja, D. Stanley, L. Theisen, A. Frawley, P. Pepmiller, L. Medsker, and P. Nagel, *Nucl. Phys. A* **351**, 509 (1981).
- [70] A. Zeller, G. Hickey, D. Weisser, D. Hebbard, and B. Robson, *Nucl. Phys. A* **301**, 130 (1978).
- [71] T. Motobayashi, I. Kohno, T. Ooi, and S. Nakajima, *Nucl. Phys. A* **331**, 193 (1979).
- [72] F. W. Prosser, R. A. Racca, K. Daneshvar, D. F. Geesaman, W. Henning, D. G. Kovar, K. E. Rehm, and S. L. Tabor, *Phys. Rev. C* **21**, 1819 (1980).
- [73] G. Benzoni, F. Azaiez, G. I. Stefan, S. Franchoo, S. Battacharyya, R. Borcea, A. Bracco, L. Corradi, D. Curien, G. De France, Z. Dombradi, E. Fioretto, S. Grevy, F. Ibrahim, S. Leoni, D. Montanari, G. Mukherjee, G. Pollarolo, N. Redon, P. H. Regan *et al.*, *Eur. Phys. J. A* **45**, 287 (2010).
- [74] F. C. L. Crespi, A. Bracco, R. Nicolini, D. Mengoni, L. Pellegrini, E. G. Lanza, S. Leoni, A. Maj, M. Kmiecik, R. Avigo, G. Benzoni, N. Blasi, C. Boiano, S. Bottoni, S. Brambilla, F. Camera, S. Ceruti, A. Giaz, B. Million, A. I. Morales *et al.*, *Phys. Rev. Lett.* **113**, 012501 (2014).
- [75] L. Pellegrini, A. Bracco, F. Crespi, S. Leoni, F. Camera, E. Lanza, M. Kmiecik, A. Maj, R. Avigo, G. Benzoni, N. Blasi, C. Boiano, S. Bottoni, S. Brambilla, S. Ceruti, A. Giaz, B. Million, A. Morales, R. Nicolini, V. Vandone *et al.*, *Phys. Lett. B* **738**, 519 (2014).
- [76] H. G. Bohlen, H. Ossenbrink, H. Lettau, and W. von Oertzen, *Z. Phys. A* **320**, 237 (1985).
- [77] A. W. Obst, D. L. McShan, and R. H. Davis, *Phys. Rev. C* **6**, 1814 (1972).
- [78] S. Salém-Vasconcelos, E. M. Takagui, M. J. Bechara, K. Koide, O. Dietzsch, A. B. Nuevo, Jr., and H. Takai, *Phys. Rev. C* **50**, 927 (1994).
- [79] J. Orloff and W. W. Daehnick, *Phys. Rev. C* **3**, 430 (1971).
- [80] A. Lépine, C. Volant, M. Conjeaud, S. Harar, and E. Da Silveira, *Nucl. Phys. A* **289**, 187 (1977).
- [81] H. G. Bohlen, K. D. Hildenbrand, A. Gobbi, and K. I. Kubo, *Z. Phys. A* **273**, 211 (1975).
- [82] M. C. Mermaiz, E. R. Chavez-Lomeli, J. Barrette, B. Berthier, and A. Greiner, *Phys. Rev. C* **29**, 147 (1984).
- [83] J. Alves, P. Gomes, J. Lubian, L. Chamon, D. Pereira, R. Anjos, E. Rossi, C. Silva, M. Alvarez, G. Nobre, and L. Gasques, *Nucl. Phys. A* **748**, 59 (2005).
- [84] E. Takagui, G. Satchler, H. Takai, K. Koide, and O. Dietzsch, *Nucl. Phys. A* **514**, 120 (1990).
- [85] J. J. Kolata, E. F. Aguilera, F. D. Becchetti, Y. Chen, P. A. DeYoung, H. García-Martínez, J. D. Hinnefeld, J. H. Lupton, E. Martinez-Quiroz, and G. Peaslee, *Phys. Rev. C* **69**, 047601 (2004).
- [86] A. Di Pietro, G. Randisi, V. Scuderi, L. Acosta, F. Amorini, M. J. G. Borge, P. Figuera, M. Fisichella, L. M. Fraile, J. Gomez-Camacho, H. Jeppesen, M. Lattuada, I. Martel, M. Milin, A. Musumarra, M. Papa, M. G. Pellegriti, F. Perez-Bernal, R. Raabe, F. Rizzo *et al.*, *Phys. Rev. Lett.* **105**, 022701 (2010).
- [87] P. K. Sahu, A. Saxena, R. K. Choudhury, B. K. Nayak, D. C. Biswas, L. M. Pant, R. G. Thomas, and Y. S. Sawant, *Phys. Rev. C* **68**, 054612 (2003).
- [88] K. S. Toth, J. L. C. Ford, G. R. Satchler, E. E. Gross, D. C. Hensley, S. T. Thornton, and T. C. Schweizer, *Phys. Rev. C* **14**, 1471 (1976).
- [89] A. Shrivastava, S. Kailas, P. Singh, A. Chatterjee, A. Navin, A. Samant, V. Ramdev Raj, S. Mandal, S. Datta, and D. Awasthi, *Nucl. Phys. A* **635**, 411 (1998).
- [90] C. Fulmer, S. Mukhopadhyay, G. Satchler, R. Auble, J. Ball, F. Bertrand, E. Gross, and D. Hensley, *Nucl. Phys. A* **385**, 83 (1982).
- [91] R. Linares, C. C. Seabra, V. A. B. Zagatto, V. Scarduelli, L. Gasques, L. C. Chamon, B. R. Gonçalves, D. R. Mendes Junior, and A. Lépine-Szily, *Phys. Rev. C* **101**, 014611 (2020).
- [92] T. Yamaya, O. Satoh, S. M. Morita, K. Kotajima, K. Hasegawa, T. Shinozuka, and M. Fujioka, *Phys. Rev. C* **37**, 2585 (1988).
- [93] S. M. Sterbenz, Elastic scattering of $^{14}\text{C} + ^{12}\text{C}$, $^{14}\text{C} + ^{16}\text{O}$, and $^{14}\text{C} + ^{18}\text{O}$, Ph.D. thesis, Yale University, 1987.
- [94] O. Hansen, F. Videbaek, E. Flynn, J. Peng, and J. Cizewski, *Nucl. Phys. A* **364**, 144 (1981).
- [95] F. Videbaek, O. Hansen, B. Nilsson, E. Flynn, and J. Peng, *Nucl. Phys. A* **433**, 441 (1985).
- [96] W. Mayer, D. Pereira, K. E. Rehm, H. J. Scheerer, H. J. Körner, G. Korschinek, W. Mayer, P. Sperr, S. C. Pieper, and R. D. Lawson, *Phys. Rev. C* **26**, 500 (1982).
- [97] L. Yang, C. J. Lin, H. Yamaguchi, J. Lei, P. W. Wen, M. Mazzocco, N. R. Ma, L. J. Sun, D. X. Wang, G. X. Zhang, K. Abe, S. M. Cha, K. Y. Chae, A. Diaz-Torres, J. L. Ferreira, S. Hayakawa, H. M. Jia, D. Kahl, A. Kim, M. S.

- Kwag, M. La Commara, R. Navarro Pérez, C. Parascandolo, D. Pierroutsakou, J. Rangel, Y. Sakaguchi, C. Signorini, E. Strano, X. X. Xu, F. Yang, Y. Y. Yang, G. L. Zhang, F. P. Zhong, and J. Lubian, *Phys. Lett. B* **813**, 136045 (2021).
- [98] E. F. Aguilera, E. Martinez-Quiroz, D. Lizcano, A. Gómez-Camacho, J. J. Kolata, L. O. Lamm, V. Guimarães, R. Lichtenhäler, O. Camargo, F. D. Becchetti, H. Jiang, P. A. DeYoung, P. J. Mears, and T. L. Belyaeva, *Phys. Rev. C* **79**, 021601(R) (2009).
- [99] C. J. Lin, J. C. Xu, H. Q. Zhang, Z. H. Liu, F. Yang, and L. X. Lu, *Phys. Rev. C* **63**, 064606 (2001).
- [100] A. Barioni, J. C. Zamora, V. Guimarães, B. Paes, J. Lubian, E. F. Aguilera, J. J. Kolata, A. L. Roberts, F. D. Becchetti, A. Villano, M. Ojaruega, and H. Jiang, *Phys. Rev. C* **84**, 014603 (2011).
- [101] K. Wang, Y. Y. Yang, A. M. Moro, V. Guimarães, J. Lei, D. Y. Pang, F. F. Duan, J. L. Lou, J. C. Zamora, J. S. Wang, Z. Y. Sun, H. J. Ong, X. Liu, S. W. Xu, J. B. Ma, P. Ma, Z. Bai, Q. Hu, X. X. Xu, Z. H. Gao *et al.* (RIBLL Collaboration), *Phys. Rev. C* **103**, 024606 (2021).
- [102] E. Muskat, J. Carter, R. Fearick, and V. Hnizdo, *Nucl. Phys. A* **581**, 42 (1995).
- [103] S. Verma, J. J. Das, A. Jhingan, K. Kalita, S. Barua, K. S. Golda, N. Madhavan, P. Sugathan, S. Nath, T. Varughese, J. Gehlot, S. Mandal, Ranjit, P. K. Sahu, B. John, B. K. Nayak, V. Jha, A. Saxena, S. K. Datta, and R. Singh, *Eur. Phys. J. A* **44**, 385 (2010).
- [104] A. Pakou, A. Musumarra, D. Pierroutsakou, N. Alamanos, P. Assimakopoulos, N. Divis, G. Doukelis, A. Gillibert, S. Harissopoulos, G. Kalyva, M. Kokkoris, A. Lagoyannis, T. Mertzimekis, N. Nicolis, C. Papachristodoulou, G. Perdikakis, D. Roubos, K. Rusek, S. Spyrou, and C. Zarkadas, *Nucl. Phys. A* **784**, 13 (2007).
- [105] E. Benjamim, A. Lépine-Szily, D. Mendes Junior, R. Lichtenhäler, V. Guimarães, P. Gomes, L. Chamon, M. Hussein, A. Moro, A. Arazi, I. Padron, J. Alcantara Nuñez, M. Assunção, A. Barioni, O. Camargo, R. Denke, P. de Faria, and K. Pires, *Phys. Lett. B* **647**, 30 (2007).
- [106] C. Beck, N. Keeley, and A. Diaz-Torres, *Phys. Rev. C* **75**, 054605 (2007).
- [107] K. Bodek, M. Hugi, J. Lang, R. Müller, E. Ungricht, K. Jankowski, W. Zipper, L. Jarczyk, A. Strzałkowski, G. Willim, and H. Witała, *Nucl. Phys. A* **339**, 353 (1980).
- [108] N. Keeley, S. Bennett, N. Clarke, B. Fulton, G. Tungate, P. Drumm, M. Nagarajan, and J. Lilley, *Nucl. Phys. A* **571**, 326 (1994).
- [109] S. Santra, S. Kailas, K. Ramachandran, V. V. Parkar, V. Jha, B. J. Roy, and P. Shukla, *Phys. Rev. C* **83**, 034616 (2011).
- [110] S. Kox, A. Gamp, C. Perrin, J. Arvieux, R. Bertholet, J. F. Bruandet, M. Buenerd, R. Cherkaoui, A. J. Cole, Y. El-Masri, N. Longequeue, J. Menet, F. Merchez, and J. B. Viano, *Phys. Rev. C* **35**, 1678 (1987).
- [111] A. Nadasen, M. McMaster, M. Fingal, J. Tavormina, P. Schwandt, J. S. Winfield, M. F. Mohar, F. D. Becchetti, J. W. Jänecke, and R. E. Warner, *Phys. Rev. C* **39**, 536 (1989).
- [112] J. Bruandet, *J. Phys. Colloques* **47**, C4-125 (1986).
- [113] L. W. Townsend and J. W. Wilson, *Phys. Rev. C* **37**, 892 (1988).
- [114] C. Mahaux, H. Ngô, and G. Satchler, *Nucl. Phys. A* **449**, 354 (1986).